https://doi.org/10.1038/s44298-025-00163-4

K5 polysaccharides inhibit SARS-CoV-2 infection by preventing spike-proteolytic priming

Maria Milanesi[1], Chiara Urbinati[1], Liv Zimmermann[2,3], Pasqua Oreste[4], Alberto Zani[5], Arnaldo Caruso[5], Francesca Caccuri[5], Vibor Laketa[6,7], Petr Chlanda[2,3], Rebecca C. Wade[8,9,10] ✉, Marco Rusnati[1,11] ✉ & Giulia Paiardi[8,9] ✉

SARS-CoV-2 spike glycoprotein is a promising drug target due to its crucial role in viral infection. Heparin, a long linear polysaccharide that inhibits SARS-CoV-2 infection by acting on spike, has limited antiviral applications due to its anticoagulant effect. *E. coli* K5 polysaccharides share the same structure as the heparin precursor and can be chemically modified to be devoid of anticoagulant activity. Here, biochemical assays and computer simulations reveal that K5 with high degree of sulfation at O- (K5OSH) or N- and O-positions (K5NOSH) bind spike with higher affinity than heparin, preventing its binding to ACE2 and furin cleavage. This mechanism is supported by cell syncytia assays showing that K5OSH and K5NOSH inhibit viral infection by blocking membrane fusion. Infection assays for SARS-CoV-2 Wuhan-Hu-1 and Omicron BA.1 variants corroborate their antiviral activity. These results support the therapeutic potential of K5OSH and K5NOSH against SARS-CoV-2, with K5OSH displaying more promising activity profile.

Since 2020, the COVID-19 pandemic caused by the severe acute respiratory syndrome coronavirus 2 (SARS-CoV-2) has heavily affected the lives of people all around the world. Despite the development of efficacious vaccines, surveillance systems, and personal protective equipment reducing the spread of infection, SARS-CoV-2 continues to result in serious symptoms, and it undergoes constant and rapid evolution of novel variants. Therefore, the development of broad-spectrum antiviral agents against SARS-CoV-2 is of high importance[1].

SARS-CoV-2 single-stranded positive-sense RNA virions are spherical with a diameter of 91 ± 11 nm and composed of four main structural proteins: spike glycoprotein (spike), envelope (E), membrane (M), and nucleocapsid (N) protein[2]. The spike is a homotrimeric class I fusion glycoprotein composed of S1 and S2 subunits that are respectively, responsible for the attachment of the virion to the host cell receptor via its receptor-binding domain (RBD) and the fusion with the host-cell membrane[2,3]. The RBD adopts an open-active or closed-inactive conformation. The RBD in the open-active conformation exposes the receptor binding motif (RBm), mediating the interaction with the host angiotensin-converting enzyme 2 (ACE2) receptor. Conversely, in the closed-inactive conformation, the RBm is shielded, hindering the binding to ACE2[4–7]. SARS-CoV-2 mediated membrane fusion requires sequential cleavage of S, which harbors a polybasic sequence that is cleaved at the S1/S2 site by furin during trafficking in a producer cell[3,8]. Once the spike has bound to the ACE2 receptor, it undergoes a second cleavage at the S2' site by transmembrane protease serine 2 (TMPRSS2) at the plasma membrane or by cathepsins in the late endosomes. Upon S2' cleavage, the S2 fusion peptide is liberated, and fusion of the viral and host membranes takes place[3,8–13].

SARS-CoV-2 can infect a broad range of tissues and, depending on the available proteases, it either fuses with the plasma membrane or with the endosomal membrane. Endosomal SARS-CoV-2 entry is supported by heparan sulfate (HS) proteoglycans (HSPGs), co-receptors expressed on the host cell[14–16]. HSPG consists of a core protein that carries multiple

[1]Macromolecular Interaction Analysis Unit, Section of Experimental Oncology and Immunology, Department of Molecular and Translational Medicine, Brescia, Italy. [2]Schaller Research Group, Department of Infectious Diseases- Virology, Heidelberg University, Heidelberg, Germany. [3]BioQuant, Heidelberg University, Heidelberg, Germany. [4]Glycores 2000 S.r.l, Milan, Italy. [5]Section of Microbiology, Department of Molecular and Translational Medicine, University of Brescia, Brescia, Italy. [6]Department of Infectious Diseases, Virology, Medical Faculty Heidelberg, Heidelberg University, Heidelberg, Germany. [7]German Center for Infection Research (DZIF), Partner Site Heidelberg, Heidelberg, Germany. [8]Molecular and Cellular Modeling Group, Heidelberg Institute for Theoretical Studies (HITS), Heidelberg, Germany. [9]Zentrum für Molekulare Biologie der Universität Heidelberg (ZMBH), DKFZ-ZMBH Alliance, Heidelberg, Germany. [10]Interdisciplinary Center for Scientific Computing (IWR), Heidelberg University, Heidelberg, Germany. [11]Consorzio Interuniversitario Biotecnologie (CIB), Unit of Brescia, Brescia, Italy. ✉e-mail: rebecca.wade@h-its.org; marco.rusnati@unibs.it; giulia.paiardi@h-its.org

polysulfated glycosaminoglycans (GAG) chains. SARS-CoV-2 binding to host cell HSPGs is mainly driven by electrostatic forces involving the sulfate and carboxyl groups of HS and the positively charged amino acid residues in the spike protein basic domains. HS binds along a partially grooved basic channel on spike spanning from the RBD in one subunit to the S1/S2 basic domain of the adjacent subunit[17]. HS binding promotes spike interaction with the host cell receptor ACE2, stabilizing the ternary complex and triggering structural rearrangement of the spike S2' cleavage site[14,16–19]. SARS-CoV-2 variants of concern, in particular Omicron BA.1, have an increased net charge in spike, leading to enhanced dependence on HS for viral attachment and infection[17,20–23]. Treatment of cells with HS analogs, such as unfractionated or low molecular weight heparin or other polysulfated GAGs reduces SARS-CoV-2 infection[18,24–26]. This is explained by heparin binding to the same basic groove path on spike, preventing binding to HS while exerting mechanistic and allosteric effects that block ACE2 interaction and the subsequent entry[20]. However, the use of heparin as a SARS-CoV-2 antiviral has been restricted because its anti-coagulant properties can cause adverse side effects in COVID-19 patients (see Table S1). Therefore, chemically modified heparin analogs with reduced anti-coagulant effects offer a promising strategy for improving COVID-19 outcomes.

Capsular K5 polysaccharides produced by *E. coli* share the same structure as the biosynthetic precursor of heparin/HS and can be chemically or enzymatically modified to resemble heparin or HS structures[27]. Sulfated K5 derivatives have anti-inflammatory and anti-adhesive effects, no cell toxicity, reduced anti-prothrombin time (APTT) and a negligible anti-coagulant effect compared to heparin (Table S2). Due to their better pharmacological properties, sulfated K5 derivatives present an attractive option for antiviral agents. Chemical modifications aim at tailoring their sulfation degree and pattern, including N-deacetylation/N-sulfation and/or O-sulfation, while enzymatic modifications are required for the conversion of GlcA into IdoA (C5 epimerization)[27–29]. Non-epimerized K5 derivatives resemble HS structures, while K5 epimerized compounds have a heparin-like structure[27]. Previous studies showed that sulfated K5s inhibit the infection of a variety of viruses that utilize HSPGs as receptors for cell entry by mimicking the binding interactions of HS, thereby competitively blocking viral access to these host-cell co-receptors[27]. The antiviral effect of sulfated K5 derivatives on SARS-CoV-2 remains to be investigated.

In this work, we leveraged atomic-detail knowledge of the mechanistic effects of heparin and HS on spike to guide the screening of non-epimerized, variably sulfated K5 derivatives against the SARS-CoV-2 Wuhan-Hu-1 and Omicron BA.1 variants by applying a multidisciplinary approach combining computational molecular modeling and simulation with biochemical and cell-based assays (Figure S1).

Results

The atomic-level insights obtained from simulations of spike-heparin complexes[20] guided the selection of variably sulfated K5 derivatives as potential antiviral candidates targeting the SARS-CoV-2 spike. Specifically, non-epimerized variably sulfated K5 derivatives lacking the active pentasaccharide required for ATIII-dependent anti-coagulant effect were engineered to compete with HS for binding along the spike basic groove while preserving a sulfation pattern capable of inducing structural rearrangements that hinder ACE2 binding. The starting K5 polysaccharide (K5) was used as a negative control having already been successfully used to this aim for other heparin-binding proteins[30] and based on atomic-level insights indicating that it would not bind to spike due to the lack of sulfated groups.

K5OSH and K5NOSH bind to spike and exhibit higher activity than heparin

Preliminary screening of a library of K5 derivatives was conducted using biochemical assays to accelerate their evaluation and selection. K5 derivatives (Fig. 1a) were assessed for their ability to bind the Wuhan-Hu-1 spike using MST[31,32]. All the sulfated K5 derivatives tested and heparin, but not K5, bind to spike in the preliminary binding check procedure (Figure S2). Dose-dependent assays performed on spike-binding GAGs showed that K5 with a high degree of sulfation in O positions (K5OSH) or both N and O positions (K5NOSH) have the highest binding affinity for spike, with dissociation constants (K_d) of 53.1 ± 7.4 and 36.0 ± 9.8 μM, respectively. K5 with a low degree of sulfation at O positions (K5OSL), both N and O positions (K5NOSL), N-sulfated K5 (K5NS) and heparin have lower binding affinities, with K_d values ranging from 0.2 to 1.5 mM (Fig. 1b and Table 1). Notably, the K_d value calculated for spike/heparin binding is comparable to previously reported data[33].

A SPR competitive binding assay was performed to test the ability of sulfated K5 to prevent spike/HS binding. The HSPGs-analogue heparin was immobilized on an SPR biosensor. All sulfated K5 derivatives tested inhibit in a dose-dependent manner the binding of spike to surface-immobilized heparin (Fig. 1c). K5 exert a very limited inhibitory effect only at very high doses (IC_{50} = 104.2 ± 4.4 nM). Heparin and K5NS exhibit modest inhibitory potency (IC_{50} = 29.3 ± 15.5 and 22.3 ± 11.4 nM, respectively), while K5OSL and K5NOSL have significantly higher inhibitory potency (IC_{50} = 1.40 ± 1.0 and 2.65 ± 1.60 nM, respectively). K5OSH and K5NOSH are the strongest heparin antagonists (IC_{50} = 0.2–0.3 nM range) (Table 1). Next, the ability of K5OSH and K5NOSH to inhibit the binding of the spike RBD to ACE2 immobilized onto a SPR biosensor was examined. At the concentrations examined, both K5 and heparin poorly inhibits spike RBD-ACE2 binding, while K5NOSH and K5OSH exhibit a stronger inhibition with IC_{50} values equal to 4700 ± 970 and 6300 ± 2200 nM, respectively (Fig. 1d and Table 1). Despite previous studies suggesting a direct binding of heparin to ACE2[15], neither heparin nor the sulfated K5 derivatives bound to ACE2 when injected onto the biosensor (Figure S3).

Spike cleavage at the S1/S2 site mainly occurs in the Golgi apparatus. Nevertheless, this intracellular cleavage can be partial, requiring extracellular furin to cleave the remaining virions[3,8,11,12,20,34]. At the concentrations examined, heparin, but not K5, inhibits furin-mediated S1/S2 spike cleavage in vitro[20,35]. In the same experimental conditions, K5OSH and K5NOSH exhibit similar potency to heparin (Fig. 1e and Table 1).

Collectively, these data indicate that K5OSH and K5NOSH could act as HS antagonists with higher activity than heparin. Since these GAGs differ in length and composition, we normalized the ID_{50} values to the concentration per repeating disaccharide unit (Table S4). Comparison of these normalized values with those based on total GAGs concentration consistently confirmed the superior inhibitory potency of K5OSH and K5NOSH as HSPGs antagonists over heparin (Figure S4). Consequently, we investigated the mechanisms of action and the antiviral efficacy of these two promising K5 derivatives.

K5OSH and K5NOSH act on the spike through direct and allosteric effects

We carried out a total of 18μs of molecular dynamics (MD) simulations of four systems consisting of models of the Wuhan-Hu-1 spike fully glycosylated in either the closed-inactive or the open-active conformation in complex with three K5OSH or K5NOSH chains (Figure S5). Simulations of the spike in both open and closed conformations were performed to reflect the mixture of these states present in the batches used for the biochemical assays as well as on the SARS-CoV-2 virion. The results were compared with those of our previous simulations of spike-heparin complexes[20].

All simulated systems converged to stable structural ensembles within ~400 ns, as shown by the root mean square deviation (RMSD) relative to each starting structure (Figure S6–S9). Compared to the complex with heparin, the subunits of the closed spike with K5OSH (Figure S6) and of the open spike with K5NOSH (Figure S8) have approximately 1 and 2 Å higher RMSD, respectively. In agreement, the root mean square fluctuations (RMSF) show increased values for the N-terminal domain (NTD) and RBD of the closed-spike subunits (Figure S10) and for the up-RBD of the open-spike complexed upon binding of both K5 derivatives (Figure S11). The K5OSH and K5NOSH chains maintain H-bonding interactions primarily with the cationic residues of the NTD and S1/S2 of one spike subunit (subunit *n*) and with cationic residues in the RBD of the adjacent spike subunit (subunit $n + 1$) with either inactive or active spike bound (Figs. 2a,

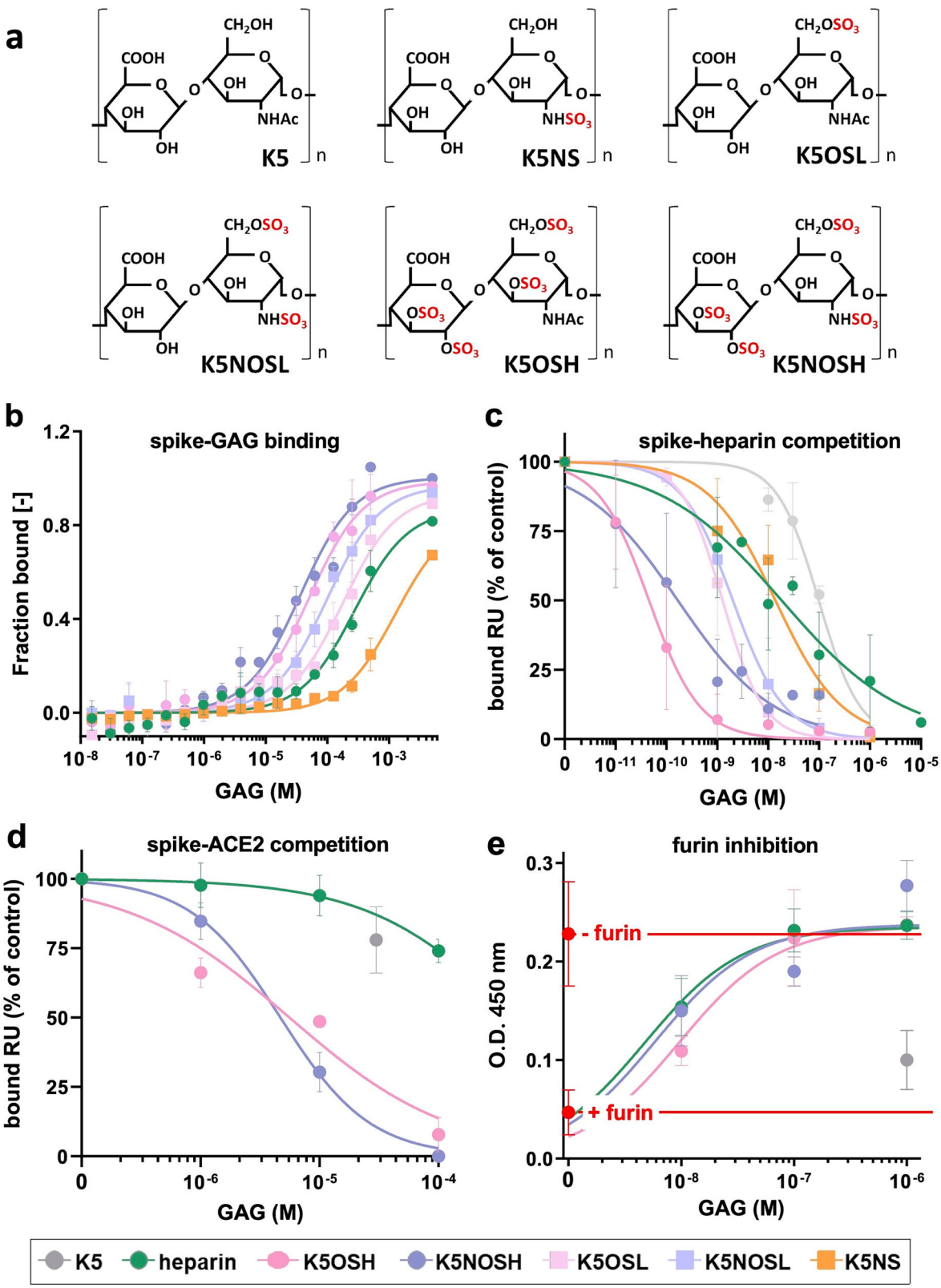

b, 3a, b and Table S5–S7). In the closed spike models, the residues involved in the binding of the two K5 derivatives are conserved and similar to those involved in binding heparin (Table S5–S6). In the open spike models, K5OSH and K5NOSH lie along the basic groove path of the active spike, although interactions with residues in the NTD and RBD significantly differ compared to heparin (Table S5–S7).

In closed spike simulations, the distances between the RBD-Loop4 loops (centroids of residues 495–516) of two adjacent spike subunits were monitored along the trajectories. The binding of K5OSH significantly reduces while K5NOSH increases the average distance between the centroids compared to heparin (Fig. 2c, Figure S12). The absence of direct contact between the RBD-Loop4 and the sulfated K5 derivatives indicates

Fig. 1 | Measurements of effects of sulfated K5 derivatives on spike show K5OSH and K5NOSH outperform heparin in binding and inhibition. a Predominant composition of the disaccharide unit present in sulfated K5 derivatives is shown (see Table S2–S3 for more details). Disaccharides are represented in their ionic form (sodium salt is the common counterion). **b** Fraction of spike bound to GAG at increasing concentrations of the indicated GAGs as measured by MST. **c** Inhibition of the interaction of immobilized heparin with spike by increasing concentrations of the indicated GAGs as measured by SPR. **d** Inhibition of the binding of spike RBD to immobilizedACE2 at increasing concentrations of the indicated GAGs as measured by SPR. For panel C and D, the responses are plotted as a percentage of the binding of spike in the absence of GAG. **e** Inhibition of cleavage of a peptide fragment containing the S_1/S_2 basic domain of spike by increasing concentrations of the indicated GAGs. The peptide was left untreated (- furin) or exposed to furin (25 ng/well) (+ furin) (red points and lanes) and after incubation in the absence and the presence of the GAG, spike cleavage was evaluated by optical density (O.D.) measurements as described in Experimental Procedures. –furin *vs* + furin: P value < 0.00001. Each point is the mean ± standard deviation (sd) of three to ten separate determinations (see Table 1 for more details).

Table 1 | Comparison of measured binding affinity and IC_{50} values of heparin and the K5 derivatives

GAG	K_d ± sd (μM)	IC_{50} ± sd (nM)		
	MST assay: spike affinity binding	SPR assay: spike-heparin interaction inhibition	SPR assay: spike-ACE2 interaction inhibition	Colorimetric assay: spike cleavage by furin
Heparin	355.1 ± 187 (4)	24.5 ± 18,7 (4)	>100,000 (3)	8.5 ± 2.1 (4)
K5	No binding	104,2 + 4,4 (3)	> 30,000 (3)	> 1000 (3)
K5NS	1569 ± 800 (3) *	14.4 + 4.3 (3)	nd	nd
K5OSL	204.7 ± 75.8 (3) *	3.5 ± 1.6 (3)	nd	nd
K5NOSL	1059 ± 10.3 (5) **	2.3 ± 1.2 (3)	nd	nd
K5OSH	53.1 ± 7.4 (3) *	0.09 ± 0.05 (4) *	6300 ± 2200 (3) ***	9.9 ± 6.62 (4)
K5NOSH	36.0 ± 9.8 (3) *	1.1 ± 0.7 (7) **	4700 ± 970 (3) ***	8.5 ± 2.1 (4)

Data are reported as mean ± sd. Number of replica experiments are reported in brackets. Student's *t*-test, K5 derivatives *vs* heparin: * $P < 0.05$; ** $P < 0.005$. *** $P < 0.0005$. nd stands for not determined.

that they allosterically affect the motion of this highly flexible region of spike RBD (Table S5–S6). The solvent-accessible surface area (SASA) of spike down-RBDs is significantly reduced only upon K5OSH binding (Fig. 2d, Figure S13). Similarly, SASA of S1/S2 is significantly reduced upon K5OSH binding while K5NOSH binding has a comparable effect to heparin (Fig. 2e, Figure S14). The difference in SASA at the S1/S2 site upon K5 binding is consistent with distinct interaction occupancies between K5 chains and S1/S2 residues. In the closed spike conformation, interactions of K5OSH with the S1/S2 site, and particularly with the furin cleavage target residue Arg685 are significantly more persistent than those observed with K5NOSH (Figure S15).

In open spike simulations, the K5 derivatives affect the movement of the spike up-RBD (Fig. 3a, b). The RMSD of residues 527-PKK-529, the hinge-residues responsible for the RBD movement[20], reveals stabilization of the residues of the up-RBD with K5OSH bound while K5NOSH derivatives have a comparable effect to heparin (Fig. 3c, Figure S16). Dihedral Principal Component Analysis (dPCA) highlights an altered sampling of the conformational space of the up-RBD hinge residues upon binding of K5 derivatives (Figure S17). In the presence of K5OSH, the first eigenvector describing the up-RBD motion showed overall stabilization of the domain, pointing to a potential inhibitory gating effect on the host cell-receptor binding (Fig. 3d, Figure S18).

With K5NOSH, the first eigenvector reveals that the polyanionic compounds promote the transition of the RBD from the starting "up" state to a semi-closed/closed state (Fig. 3d, Figure S18) leading to greater shielding of the up-RBm than heparin or K5OSH (Fig. 3e, Figure S19). K5OSH derivatives have an effect comparable to heparin in shielding the S1/S2 functional site of the spike up-subunit while K5NOSH derivatives have a significantly lower ability to mask this functional site (Fig. 3f, Figure S20 and Table S5).

Notably, both K5s outperform heparin in shielding the S1/S2 site of the closed subunits (S_A and S_B) on the open spike (Figure S20). The shielding effect is again reflected in the occupancy of the interactions between the positively charged residues at the S1/S2 site and the K5 chains. In the open spike monomer, the residue targeted by furin cleavage Arg685 shows an interaction occupancy ≥75% in all replicas when bound to the K5OSH chain. For the K5NOSH chain, Arg685 maintains an occupancy above 50% in all replicas (Figure S21). These results support the hypothesis that O-sulfated chains are more effective than N, O-sulfated chains in shielding the furin cleavage site of the open spike monomer.

In summary, the K5OSH derivative outperforms heparin and K5NOSH as regards spike inhibition by promoting a more compact packing and shielding of closed spike while inducing rigidification of the up-RBD in the open spike, thereby hampering the binding to ACE2 and enhancing the shielding of S1/S2. Notably, K5OSH established more stable interactions with S1/S2 residues in both closed and open conformations, with particularly persistent contacts at the furin cleavage target Arg685, thus providing more effective protection against furin-mediated cleavage, in line with our experimental results. By contrast, K5NOSH shields the RBm of spike up-subunit more effectively than heparin and K5OSH, and thereby hampers ACE2 binding. Computational studies provide a mechanistic explanation of the stronger activity of the K5 derivatives than heparin in biochemical assays, pointing to K5OSH as the most promising among the compounds tested.

K5OSH and K5NOSH inhibit SARS-CoV-2 infection by blocking S-mediated membrane fusion

Biochemical and computational assays point to the ability of K5OSH and K5NOSH to exert an antiviral effect by multiple mechanisms including competing with the host-cell HSPGs for the binding of spike, preventing the spike-proteolytic priming at the S1/S2 site, by directly shielding it, and at the S2' site by hampering the binding of spike to ACE2 and the subsequent exposure of residue R815[13,17].

To gain further insight into the mechanism of the inhibition, the effect of the K5 compounds was first tested directly on spike-mediated membrane fusion using a syncitia assay, which depends on the S2' cleavage carried out by TMPRSS2 at the plasma membrane[36]. The assay was performed on cells expressing either Wuhan-Hu-1 spike, corresponding to the biochemical and computational assays, or Omicron BA.1 spike, to evaluate the therapeutic potential of the K5 derivatives on a more recent virus variant. Using automated microscopy and machine learning-based segmentation of nuclei in spike-positive cells and spike-positive syncitia, we determined the fraction of nuclei involved in syncytia formation. Our data show that the number of Wuhan-Hu-1 spike-positive cells involved in syncytia formation using

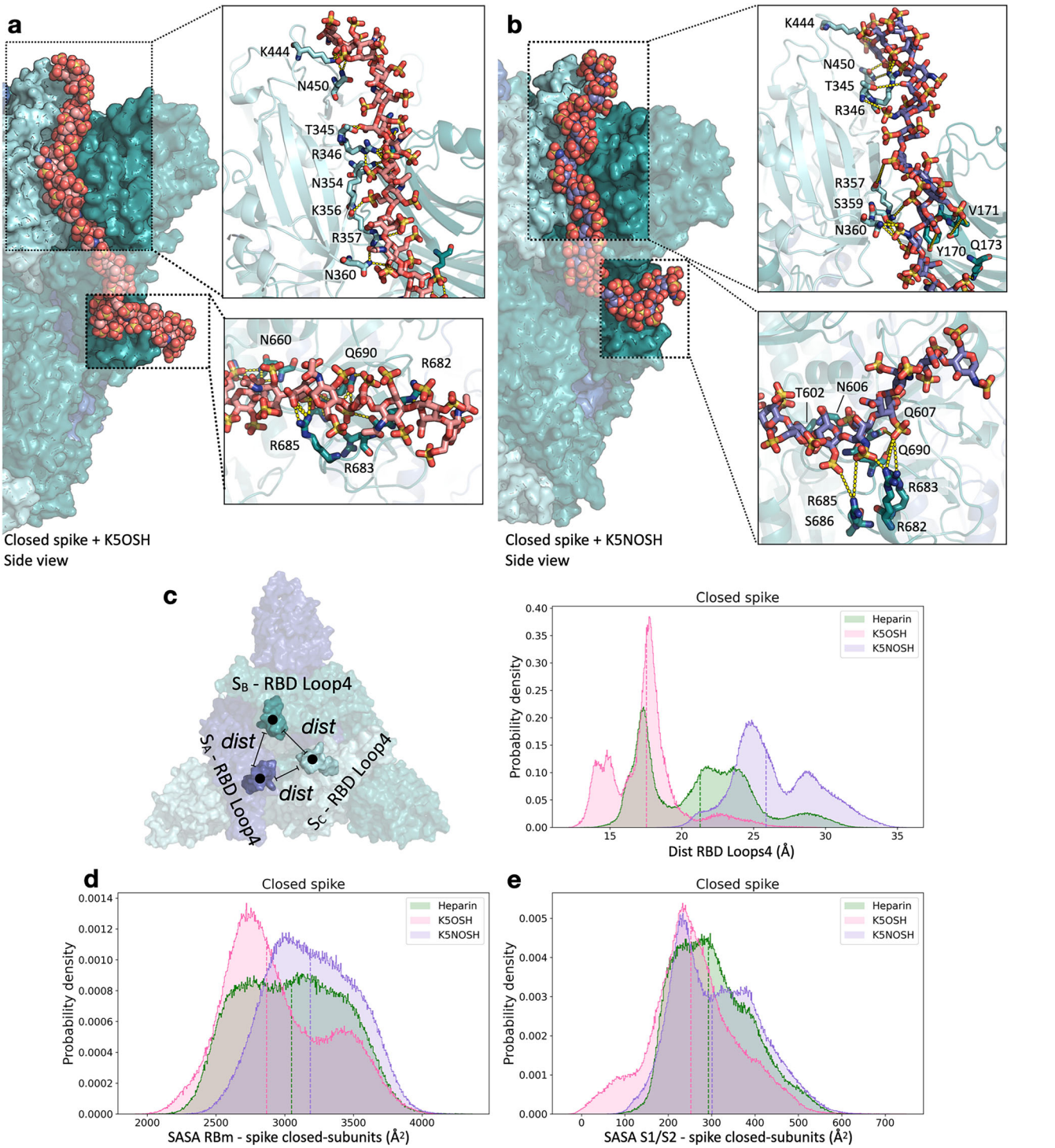

Fig. 2 | MD simulations of K5OSH and K5NOSH on the closed spike conformation reveal tighter packing of the spike subunits when K5OSH rather than heparin is bound. a, **b** Representative structures obtained after MD simulation of the spike bound to three K5OSH **a** or K5NOSH **b** chains. The S_A, S_B, and S_C spike subunits are shown as molecular surfaces in cyan, teal, and blue, respectively. The 31mer K5 chains that span from the RBD of one spike to the S1/S2 site of the adjacent subunit are shown in van der Waals sphere representation colored by element with carbons in pink and purple for K5OSH and K5NOSH, respectively. Insets show the interactions of the K5 chains with residues in the down-RBD (top) and S1/S2 sites (bottom). The spike and its interacting residues are depicted in cartoon and stick representations, respectively, and colored according to the respective subunit. H-bonds are shown as yellow dashed lines. N-glycans covalently attached to the spike are not shown for clarity. **c** To define the variation in packing of the closed spike, the distances (dist) between RBD Loop4 (centroids of residues 495-516 represented as spheres) of adjacent spike subunits were calculated. The probability density of the distances between RBD Loop4s was calculated from the converged MD trajectories for all the replicas and colored according to systems: heparin-bound (heparin in green, K5OSH in pink, K5NOSH in purple). K5OSH binding promotes a tighter packing of the closed spike. The probability distribution of the SASA for the down-RBm **d** and S1/S2 multifunctional domain **e** were calculated from the converged MD trajectories for all the replicas and colored according to systems: heparin-bound (green), K5OSH-bound (pink) and K5NOSH-bound (purple). K5OSH binding reduces the exposure of the RBm and S1/S2 with respect to the reference systems with heparin. Corresponding plots, shown as a function of time and as probability density for each replica trajectory and reference system for **c**–**e** are shown in Fig S12–14.

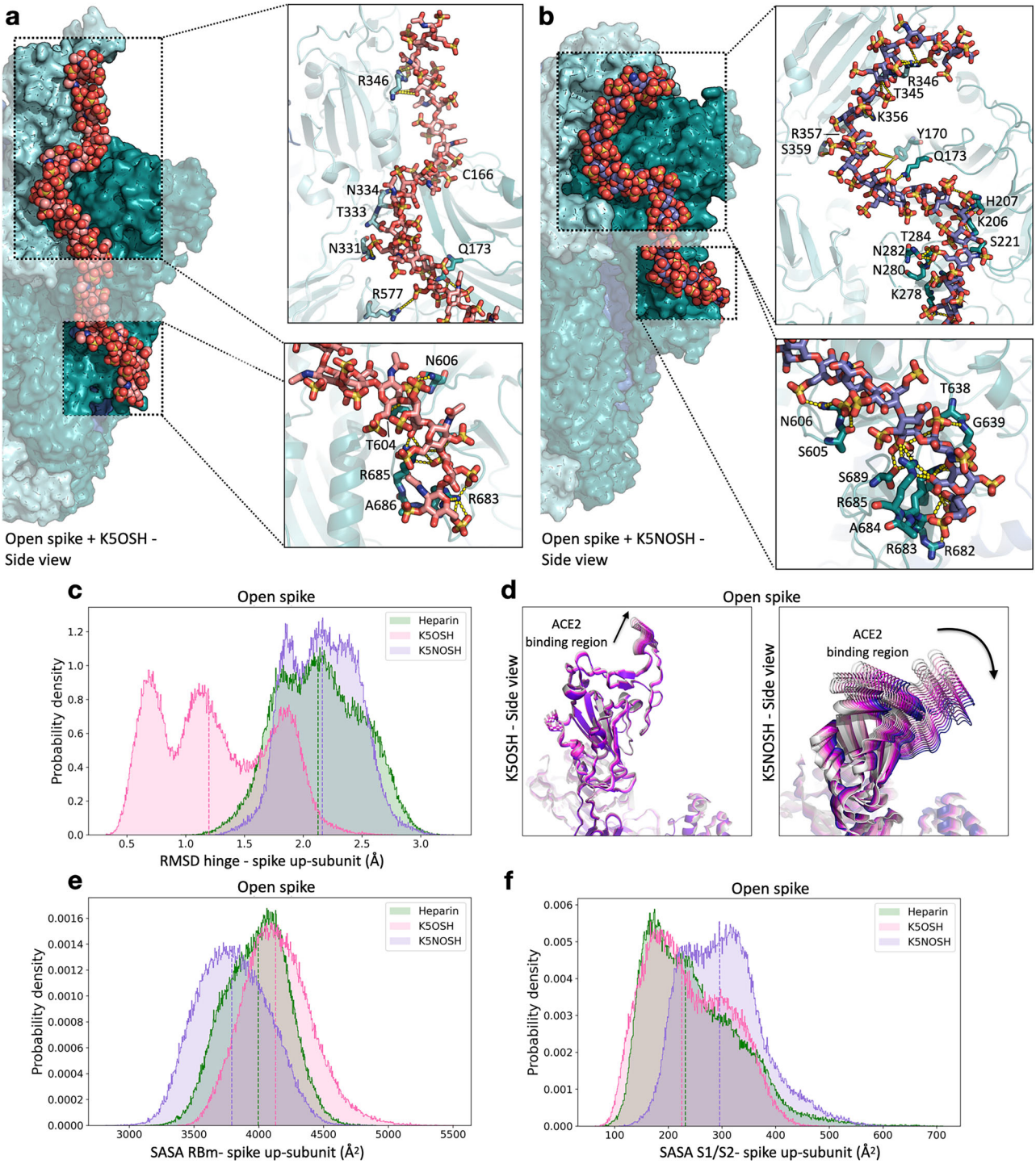

VeroE6 cells is higher than the number of Omicron BA.1 spike-positive cells (Fig. 4a, b). Syncytia contained fewer nuclei upon treatment with K5 derivatives (Fig. 4c, d). K5OSH had a statistically significant inhibitory effect on Wuhan-Hu-1 induced fusion while both K5OSH and K5NOSH significantly reduced Omicron BA.1 membrane fusion.

Finally, K5OSH and K5NOSH were examined for their antiviral activity in an infection assay using authentic SARS-CoV-2 B.1 (D614G) and Omicron BA.1 variants on VeroE6 and on A549 ACE2+ cells. Despite its lack of spike-binding capacity (Figure S2), K5 was included in the assay to assess potential off-target effects independent of direct spike binding that could occur in a complex cell-based model. Cell viability assays were conducted in the absence of the virus to calculate the half-cytotoxic concentration (CC_{50}) for the compounds. At 48 h post-treatment, all compounds exhibited no significant toxicity at concentrations up to 100 μM on VeroE6 cells (Fig. 5a). Heparin and K5OSH showed a slight cytotoxic effect at 100 μM on A549 ACE+ cells, and therefore this dose concentration was excluded from the subsequent assays (Fig. 5b). K5 was ineffective against the B.1 and BA.1 variants on both VeroE6 and A549 ACE+ cells (Fig. 5c–f). When tested against the B.1 variant, K5OSH and K5NOSH had a weak inhibitory effect on VeroE6 cells (IC_{50} = 22.00 and >10 μM, respectively) (Fig. 5c and Table 2). In A549 ACE+ cells, K5OSH exhibited stronger antiviral activity (IC_{50} = 0.21 μM) than K5NOSH and heparin (IC_{50} = 2.18 and 2.66 μM, respectively) (Fig. 5d and Table 2). When tested against the Omicron BA.1 variant, K5OSH and K5NOSH inhibited infection in both

Fig. 3 | MD simulations of K5OSH and K5NOSH on the open spike conformation show that, compared to heparin, K5OSH affects the RBD-orientation while K5NOSH alters exposure of spike binding sites. a, b Representative structures obtained after MD simulation of spike bound to three **a** K5OSH and **b** K5NOSH chains. The S_A, S_B, and S_C spike subunits are shown as surface in cyan, teal, and blue, respectively. The 31mer K5 chains that span from the RBD of one spike to the S1/S2 site of the adjacent subunit are shown in sphere representation colored by element with pink and purple representation for K5OSH and K5NOSH, respectively. Insets show the interactions between the sulfated K5 derivatives and residues in the up-RBD (top) or S1/S2 sites (bottom). The spike and its interacting residues are depicted in cartoon and stick representations, respectively, and colored according to the subunit to which they are attached. H-bonds are shown by yellow dashed lines. N-glycans covalently attached to the spike are not shown for clarity. **c** The probability density of the RMSD for the hinge region (residues 527–529) of the spike up-subunit calculated from the converged MD trajectories for all the replicas and colored according to systems (heparin in green, K5OSH in pink, K5NOSH in purple) showing that K5OSH-binding results in stabilization of the hinge region in the spike up-RBD. **d** The change in motion of the up-RBD induced by the presence of K5 derivatives is shown by the superimposition of conformations extracted at equal time intervals along the trajectories (from magenta to blue) and projected onto the first essential dynamics eigenvector with K5OSH (left) and K5NOSH (right). The RBD is shown in cartoon representation and the K5 derivatives are omitted for ease of visualization. The probability distribution of the SASA for the up-RBD RBm **e** and S1/S2 multifunctional domain **f** calculated from the converged MD trajectories for all the replicas and colored according to systems (heparin in green, K5OSH in pink, K5NOSH in purple) showing that only K5NOSH decreases the exposure of the RBD RBm whereas K5OSH has a comparable effect to heparin in shielding the exposure of the S1/S2 basic site of the up-spike subunit. Corresponding plots, shown as a function of time and as probability density for each replica trajectory and reference system for **c**–**e** are shown in Figure S16–S20.

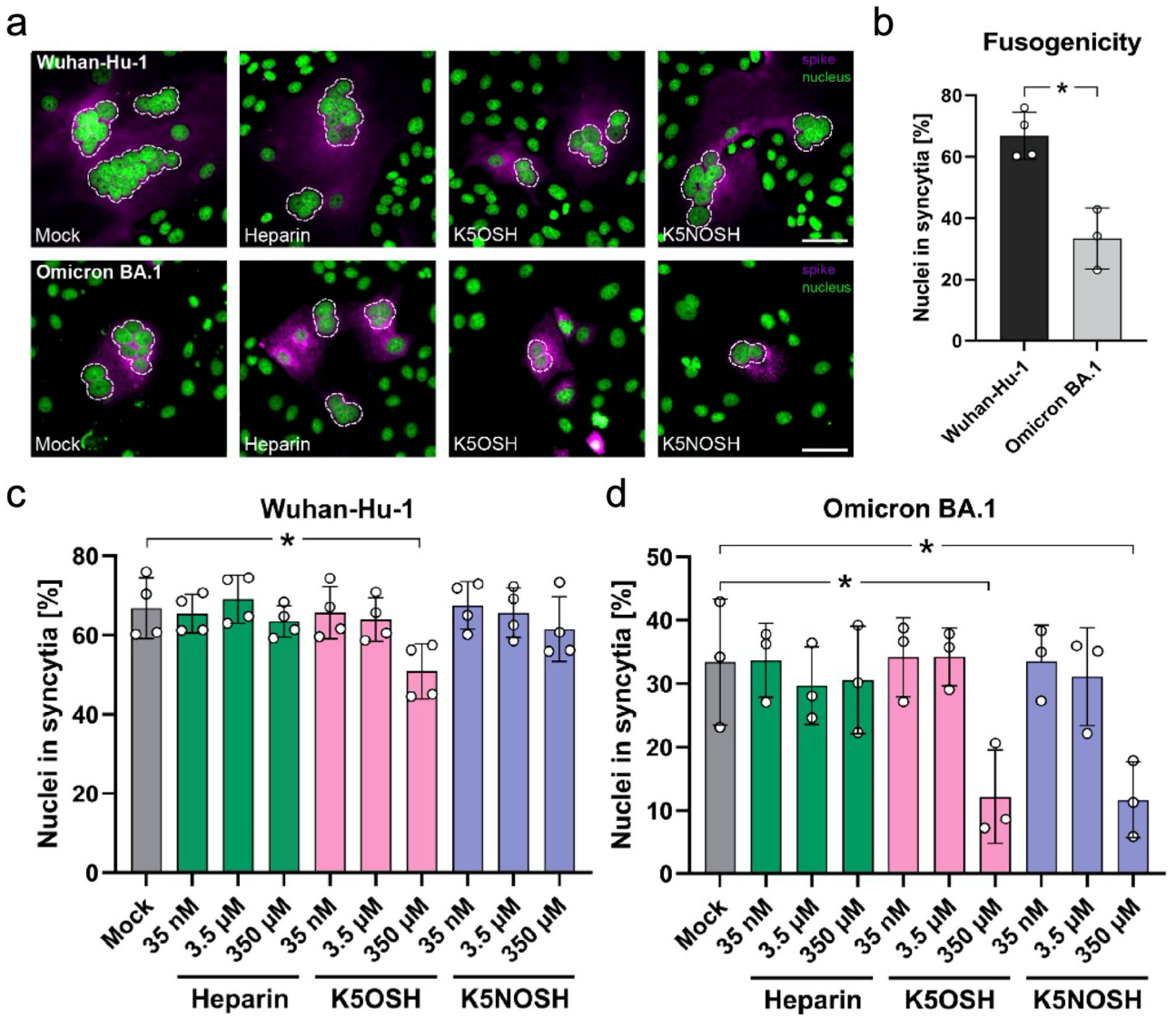

Fig. 4 | Measurements of syncytia formation show greater dose-dependent effects of K5 compounds than heparin. a Representative images of syncytia formation assay in VeroE6 cells upon treatment (350 µM) with K5 compounds. Scale bar: 50 µm. **b** Number of nuclei involved in syncytia formation is higher in Wuhan-Hu-1 spike-positive cells than in Omicron BA.1 spike-positive cells. **c** Effect of K5 compounds on syncytia formation induced by Wuhan-Hu-1 spike. **d** Effect of K5 compounds on syncytia formation induced by Omicron BA.1 spike. Only spike-positive cells were quantified. Data of four (Wuhan-Hu-1) and three (Omicron BA.1) independent experiments. Values are mean ± sd. P values determined by Welch's t-test: * $P < 0.05$; ** $P < 0.005$.

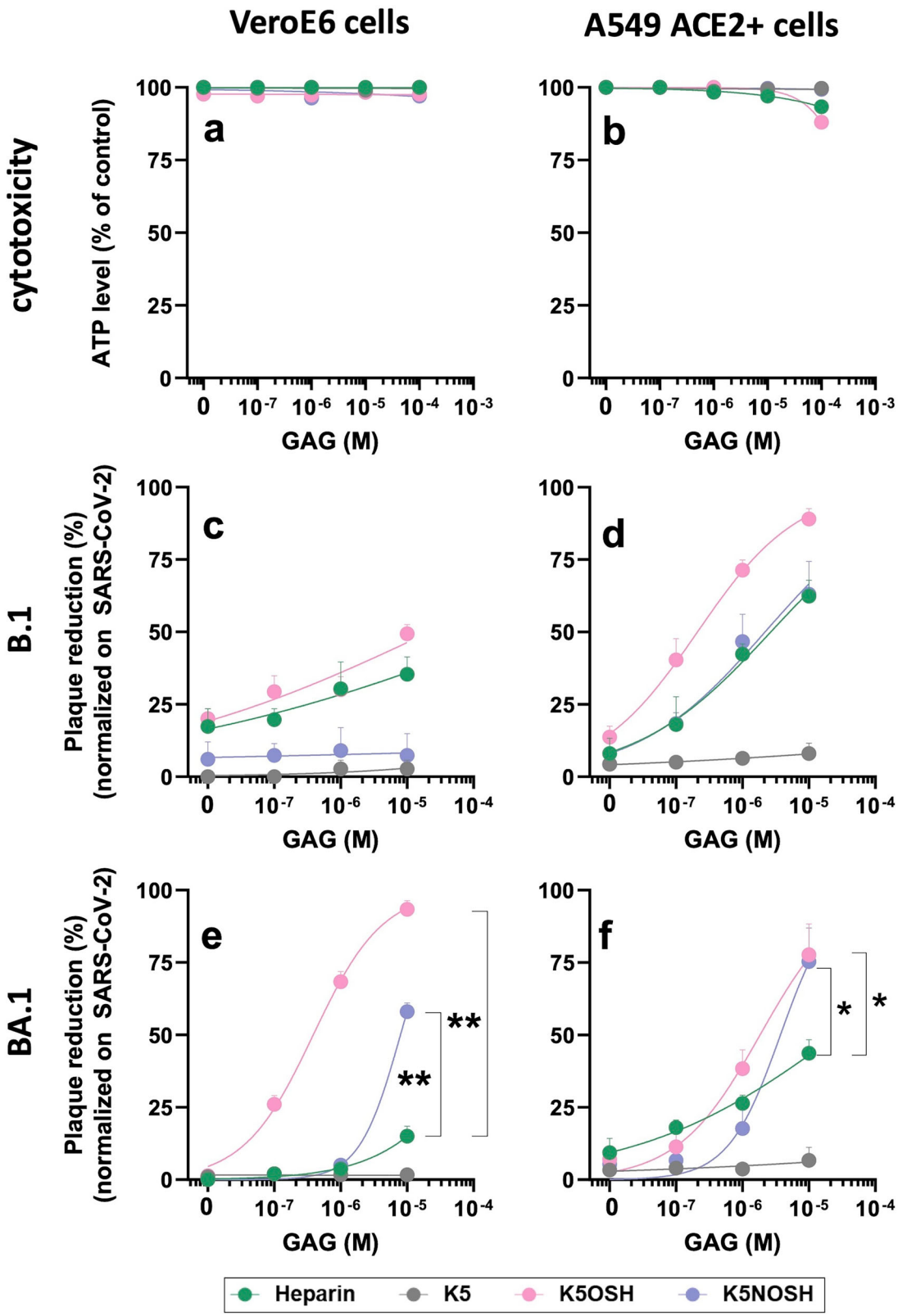

Fig. 5 | Measurements of cytotoxicity and antiviral activity against SARS-CoV-2 B.1 and Omicron BA.1 show inhibition by the K5 compounds with K5OSH showing the greatest inhibitory effect. VeroE6 cells or A549 ACE2+ cells were treated with increasing concentrations of heparin, K5, K5OSH, and K5NOSH. **a**, **b** The cells remained viable in the presence of heparin and the K5 compounds as evaluated by measuring the ATP levels. VeroE6 or A549 ACE2+ cells were infected with the B.1 **c**, **d** or Omicron BA.1 **e**, **f** isolates in the presence or the absence of increasing concentrations of heparin, K5, K5OSH, and K5NOSH. Infection was reduced in a concentration-dependent manner as shown by the percentage of plaque reduction compared to SARS-CoV-2 alone. Data are presented as the mean value ± standard error of three independent replicates. $^{*}P < 0.05$; $^{**}P < 0.005$.

Table 2 | Inhibition of SARS-CoV-2 infection in cells by heparin, K5, K5OSH, and K5NOSH

Inhibitory potency (IC_{50} ± sd, μM)				
	VeroE6 cells		A549 ACE2+ cells	
GAG	B.1	BA.1	B.1	BA.1
Heparin	456.3 ± 164.2	172.1 ± 84.1	2.66 ± 0.78	26.73 ± 6.77
K5	> 10	> 10	> 10	> 10
K5OSH	22.00 ± 4.00	0.39 ± 0.08 **	0.21 ± 0.04	1.84 ± 0.43 *
K5NOSH	> 10	7.95 ± 0.82 **	2.18 ± 0.06	3.73 ± 0.79 *

Data are the mean value ± sd of three independent replicates. In the absence of a saturation effect, IC_{50} values were calculated on the trend of the curve (Fig. 5) using GraphPrism 8.4. Student's *t*-test, IC_{50} for inhibition of BA.1 infection: K5OSN and K5NOSH *vs* heparin: $^{**}P < 0.005$ for VeroE6 cells assay and $^{*}P < 0.05$ for A549 ACE2+ cells assay.

VeroE6 cells (IC_{50} = 0.39 and 7.95 μM, respectively) and A549 ACE+ cells (IC_{50} = 1.84 and 3.73 μM, respectively) while heparin was ineffective (Fig. 5e, f and Table 2).

Collectively, our results demonstrate that K5OSH and K5NOSH exhibit stronger antiviral activity than heparin against SARS-CoV-2, with particularly pronounced effects against Omicron variant. Notably, the inhibitory potency of the sulfated derivatives (22–198 μg/ml) falls within the same range as those reported for carrageenans (5–120 μg/ml)[37,38], another class of anti-SARS-CoV-2 polysaccharides.

Discussion

Heparin has been investigated for its antiviral effect against SARS-CoV-2[24–26]. It competes with HS for binding to the basic groove path along the spike and thereby directly and allosterically hinders the binding to the host-cell receptor ACE2, spike proteolytic cleavage, and its subsequent activation[20]. However, the anti-coagulant activity of heparin has hampered its application as an antiviral agent, prompting the investigation of 'non anti-coagulant' heparins, synthetic drugs, natural polysaccharides (such as carrageenans[37,38],) and oligosaccharides as potential antivirals[33,39,40]. K5 polysaccharides derived from *E. coli* share the same structure as the HS/heparin precursors while exerting anti-inflammatory and anti-adhesive effects, and having no cell toxicity, reduced APTT, and negligible anti-Xa effects (Table S2).

Here, by leveraging the atomic-detail knowledge obtained by simulating spike-heparin and spike-HS-ACE2 complexes[17,20], we screened a library of non-epimerized variably sulfated K5 derivatives, including K5 used as a negative control, aimed at targeting the spike basic groove path that accommodates heparin/HS and competitively preventing their binding while simultaneously hindering ACE2 binding and spike proteolytic cleavage.

First, biochemical screening revealed that K5 does not bind the Wuhan-Hu-1 spike, whereas the highly sulfated derivatives K5OSH and K5NOSH are the strongest binders exhibiting K_d values 6–10 times lower than heparin, which has a lower degree of sulfation (Table S3). These findings collectively highlight the electrostatically driven nature of these molecular interactions. Based on these results, we focused on K5OSH and K5NOSH, which were shown to inhibit both furin-mediated cleavage of the spike S1/S2 site and the binding of Wuhan-Hu-1 spike-RBD to HSPGs-analogue heparin and ACE2.

Next, computational studies demonstrated that K5OSH and K5NOSH bind to the Wuhan-Hu-1 spike following the basic groove previously identified, and competing with host-cell HSPGs for binding while shielding the S1/S2 functional site, therefore preventing furin cleavage[17,20]. Strong electrostatic repulsion between K5OSH or K5NOSH (both with a net charge of -75e for a 31mer) and the ACE2 receptor binding domain (-27e), coupled with shielding of the spike RBm, inhibit the binding of the host cell receptor ACE2, thereby hampering the subsequent cleavage of S2' by TMPRSS2[13,17]. Mechanistically, K5OSH outperforms heparin and K5NOSH by promoting a tighter packing of the closed spike, higher interaction occupancy at the S1/S2 cleavage site (particularly at the target site Arg685) and rigidification of the up-RBD of the open spike, pointing to a potential inhibitory gating effect on host cell-receptor binding.

The combined interpretation of biochemical assays and computational simulations indicate that the inhibitory potency of the sulfated K5 derivatives is not solely determined by the overall degree of sulfation and/or the binding affinity for spike, but critically depend on the spatial arrangement of sulfated groups along the polysaccharide backbone. This arrangement governs chain flexibility and the ability to engage the basic groove of the spike protein. Notably, K5OSH exhibits greater conformational adaptability and reduced steric hindrance compared to K5NOSH, due to the absence of highly solvated NS groups. These findings are consistent with previous observations that 2-O and 6-O sulfation have stronger impact than N-sulfation in mediating spike binding and inducing RBD conformational changes[15,18,41]. Collectively, these structural features allow K5OSH to better accommodate the narrow basic groove, enhancing both the stability and potency of its interaction with spike.

Subsequently, an assay of syncytia, which depends on the S2' cleavage carried out by TMPRSS2 at the plasma membrane, was performed. It has been shown that syncytia formation is enhanced by TMPRSS2 and inhibited by interferon-induced transmembrane protein 1[36]. SARS-CoV-2 variants show differences in the preferred route of entry and the site of membrane fusion. The original Wuhan-Hu-1, B.1 and Delta variants are highly sensitive to Cemostat (an inhibitor of TMRSS2) and prefer to enter the cell by direct fusion with the plasma membrane[42]. In contrast, the Omicron variants are less dependent on TMPRSS2 cleavage and utilize an endocytic pathway[43,44] where both S1/S2 and S2' cleavage can be carried out by endosome-associated proteases[45,46]. Hence, the effect of K5 compounds on spikes of the Wuhan-Hu-1 and Omicron BA.1 variants was evaluated using syncytia assays in VeroE6 cells, which contain low amounts of TMPRSS2[46]. In agreement with previous reports, the expression of the Wuhan-Hu-1 spike induces more cells to form syncytia than the expression of the Omicron BA.1 variant spike protein[43]. Notably, K5OSH significantly inhibits syncytia formation induced by the Wuhan-Hu-1 spike protein. K5OSH and K5NOSH both significantly inhibit Omicron BA.1 spike-mediated VeroE6 syncytia formation at the highest used concentration. These results indicate that the K5 inhibitory mechanism is linked to the inhibition of proteolytic cleavage at the S1/S2 and S2' cleavage sites, as indicated in the computational studies.

Finally, the antiviral activity of K5OSH and K5NOSH were evaluated, alongside with K5 used as a negative control, against SARS-CoV-2 B.1 and Omicron BA.1 variants in VeroE6 and A549 ACE2+ cells, both exhibiting low levels of TMPRSS2 expression. The K5 derivatives tested exerted a stronger inhibitory activity on infection by Omicron BA.1 and K5OSH was more potent than K5NOSH at inhibiting virus infection, in line with syncytia formation assays. One explanation of the different activity of the K5 derivatives in infection assays using alternative cell types can be attributed to variations in the ratio of closed to open spikes on SARS-CoV-2 virions. In cells with low ACE2 expression, such as Vero E6 cells, spikes predominantly adopt the prefusion closed conformation[2]. Computational studies indicate that in closed spike conformation, K5OSH exhibits a higher antiviral effect compared to the other polysaccharides investigated. In contrast, the ratio between open and closed spikes is balanced in cells with higher ACE2 expression as A549 ACE2+ cells[2]. This balance explains the increased efficacy of heparin and K5NOSH, as computational studies attribute their enhanced activity to a greater effect on the open spike, although K5OSH remains the most active overall. Furthermore, since the interaction between K5 derivatives and the spike is driven by long-range electrostatic interactions, the enhanced activity of K5 derivatives against the Omicron BA.1 variant is likely due to its increased net charge compared to the Wuhan-Hu-1 spike[17,22], resulting in greater affinity for the selected K5 derivatives.

Overall, our multidisciplinary approach demonstrates that K5OSH is the most potent anti-SARS-CoV-2 agent among the compounds tested. It competes with HS for spike binding, inhibiting its proteolytic priming at S1/

S2 through direct interaction and shielding, and at S2' by preventing ACE2 binding, subsequent exposure of R815, and TMPRSS2-mediated cleavage[13,17]. Of note, K5OSH derivatives are not susceptible to heparinase I and II degradation due to their specific sulfation pattern[47]. Nevertheless, given the increased levels of cellular lyases in the plasma of COVID-19 patients with severe clinical outcomes, further experiments aimed at excluding the susceptibility of K5OSH to cell lyases would be crucial. Furthermore, since the effects of the selected K5 derivatives have been tested on only two spike variants, further experiments are needed to elucidate antiviral potential and impact on infectivity and inhibitor binding on circulating SARS-CoV-2 variants and cells overexpressing TMPRSS2. Finally, the biosafety and effectiveness of these compounds need a more detailed investigation and evaluation using animal models before pharmaceutical applications.

SARS-CoV-2 has evolved to infect the upper respiratory tract. Although inhaled nebulized heparin has been evaluated in COVID-19 patients, its systemic bioavailability restricts its use as an antiviral owing to the risk of bleeding or hemorrhagic events[48–50]. Inhaled nebulized formulations of sulfated K5 could achieve higher local drug concentrations enabling a rapid clinical response, reducing risks of degradation by cellular lyases and, most importantly, minimizing systemic side effects due to the safer profile of K5 compared to heparin[30,51]. Of note, topical administration of sulfated K5 derivatives has shown no toxicity or significant inflammation[52]. Collectively, these observations highlight the rationale for further clinical investigations of nebulized K5OSH, identified here as the most promising candidate for the prevention of SARS-CoV-2 infection.

Materials and methods

This work has been carried out by a multidisciplinary approach entailing biochemical, computational and cell-based analysis including: microscale thermophoresis and surface plasmon resonance assays to evaluate the capacity of the sulfated K5 derivatives to bind spike protein and to inhibit its binding to heparin (used as an analog of HSPGs); a furin cleavage assay to evaluate the capacity of sulfated K5 derivatives to prevent the enzymatic proteolysis of spike; all-atom MD simulations to analyze the binding mode(s) and mechanistic effects exerted by the sulfated K5 derivatives with spike; a cell syncytia formation assay to evaluate the capacity of the sulfated K5 derivatives to prevent this spike-and TMPRSS2-dependent pathological process; and an infection assay with different SARS-CoV-2 strains and cell lines to evaluate the therapeutic potential of the sulfated K5 derivatives.

Reagents

Reagents and materials were used as received, unless otherwise mentioned, and were purchased from the following: Human recombinant SARS-CoV-2 Wuhan-Hu-1 spike His-Tag protein and RBD from Sino Biological (#40592-V08B); ACE2 from Acrobiosystem (#AC2-H52H8); Bovine Serum Albumin (BSA) from Merck (#810037); Human recombinant furin from OriGene Technologies Inc. (#TP304279M); Conventional heparin (13.6 kDa - purity ≥95%) from a commercial batch of unfractionated sodium heparin from Laboratori Derivati Organici S.p.A. (#9041-08-1).

Synthesis and characterization of sulfated K5 derivatives

K5 polysaccharide was obtained by fermentation as previously described[53]. The sulfated K5 derivatives were then synthesized starting from the unsulfated K5 polysaccharide as shown schematically in Figure S22 and described in detail below.

K5NS: for N-deacetylation, ten grams of pure K5 polysaccharide were dissolved in 1000 ml of 2 M NaOH (2 N), (Merck Life sciences, Darmstad, Germany) kept at 60 °C for 24 h and then brought to room temperature and to neutral pH with 6 M HCl (6 N) (Merck Life Sciences) step by step. For N-sulfation, the solution containing the deacetylated K5 was kept at 40 °C, 16 g Na_2CO_3 (Merck Life Sciences) were added and subsequently 16 g pyridine SO_3 adduct (Merck Life Sciences) were added over a 4 h period. After 24 h, the solution was brought to room temperature and then to pH 7.5-8 with a HCl 5% solution. The product was purified from salts by diafiltration using a spiral membrane of 1000 D (Prepscale Cartridge-Millipore). The process was ended when the conductivity of the permeate was below 100 µS. The intradialysis was reduced until a polysaccharide concentration of 10% was obtained using the same dialysis system in concentration and then freeze-dried.

K5NOSH: for O-oversulfation, K5NS was dissolved in 100 ml of deionized H_2O, brought to 10 °C in a cooling bath, and then passed onto a cationic exchange resin IR120H+ (100 ml, Mer ck Life Science) maintained at 10 °C. After the passage of the sample, the resin was washed with about 3 volumes of deionized H_2O until the pH of the permeate was higher than 6. The acidic solution was then brought to pH 7 with tetrabutylammonium hydroxide (Merck Life Sciences) (15% aqueous solution), reduced to the minimum volume and freeze-dried. The tetrabutylammonium salt was dissolved in 400 ml of dimethylformamide (DMF) (Merck Life Sciences) and 35 g pyrimidin SO_3 adduct in solid form was added. The solution was kept at 50 °C for 24 h, cooled to room temperature and 3 volumes of NaCl pyrimidin SO_3 adduct saturated acetone added, then further cooled to 4 °C until complete precipitation in about 12 h. The precipitate was separated from the solvent by filtration, solubilized with the minimum amount of deionized H_2O (about 100 ml) and NaCl (Merck Life Sciences) was added until a 0.2 M concentration was reached. The solution was then brought to pH 7.5–8 with 2 N NaOH and treated with 2 volumes of acetone until complete precipitation. The precipitate was separated from the solvent by filtration, solubilized with 100 ml deionized H_2O and purified from the residual salts by ultrafiltration using a spiral membrane of 1000 D. Since during the reaction of O-sulfation the N-sulfation of the product gets partially lost, a highly O-sulfated, partially N-sulfated K5 was obtained that was subjected again to N-sulfation with the same procedure described above.

K5NOSL: the derivative was obtained as described for K5NOSH, but using 7 g of pyrimidine SO_3 adduct. A partially O-sulfated KNOS was obtained that was then subjected to the final step of N- re-sulfation.

K5OSH: 300 mg of pure K5 polysaccharide were dissolved in 50 ml of H_2O and passed over a IR120H+ column at room temperature. The column was washed with 100 ml of H_2O and the acid pH of the eluted solution was brought to pH 7 with a solution of 15% tributylammonium hydroxide (Merck Life Sciences). The solution was then concentrated and freeze-dried. The sample was dissolved in 22 ml of DMF and a further 22 ml of DMF containing 1.924 g of pyrimidin SO_3 adduct were added. This solution was kept at 50 °C under stirring for 24 h, then added with one volume of H_2O and brought to pH 7 with 5 M NaOH. To precipitate the sample, 3 volumes of acetone saturated with NaCl were added and kept at 4 °C. The precipitate was recovered by centrifugation at 5000 rpm for 10 min, resuspended in H_2O and ultrafiltered on a 1000 D cut-off membrane and finally freeze-dried.

K5OSL: this derivative was obtained as described for K5OSH, but using 7 g of pyrimidin SO_3 adduct.

The MW of the compounds was calculated by GPC/HPLC analysis on a TSK 3000 column (Tosho Bioscience, Shanghai, China) eluted with 0.15 M NaCl and a flux of 0.5 ml/min. Their purity was analyzed by Biorad protein assay (Biorad, Hercules, California, USA). Their NMR analysis is reported in Figure S23.

The concentration of the samples in the mobile phase was 0.03%. The readings were performed at 205 nm and the calculation of the parameters was performed against heparin standards with different MWs.

The Anti–Xa activity was performed with Coatest Heparin by Chromogenix (Werfen, Barcelona, Spain) and APTT activity was detected with PTT reagent (Boheringer Mannheim Roche, Basel, Switzerland), following the indications of the manufacturer.

The main structural and functional features of sulfated K5 derivatives are reported in Table S2–S3.

Biochemical studies

Microscale thermophoresis (MST) assays: spike His-tag protein (100 nM protein, molar dye:protein ratio ≈ 1:2) was labeled using the His-Tag Protein

Labeling Kit RED-tris-NTA (NanoTemper Technologies) in labeling buffer at room temperature for 30 min. in the dark and adjusted to 25 nM with phosphate-buffered saline buffer (PBS) containing 0.05% Tween 20 (PBST buffer). A two-step procedure was followed with an initial binding measurement performed on the Monolith NT.115 (NanoTemper Technologies) using the MO.Control 2 software. Samples containing spike (20 nM in PBSST) in the absence or in the presence of 15 μM of each K5 derivative were prepared, incubated for 30 min, centrifuged at 10,000 × *g* for 10 min, and loaded into Monolith NT.115 capillaries (NanoTemper Technologies) using 4 capillaries for each sample. MST was measured using a Monolith NT.115 instrument at 25 °C. The instrument parameters were adjusted to 100% LED power and medium MST power, and the MST signal of spike alone was compared to the MST signal of the complex. The signal-to-noise ratio, defined as the response amplitude (difference of MST signal of spike alone and in complex, in ‰ F_{norm} units), divided by the noise of the measurement sd of the 4 replicates was used to evaluate the quality of the binding data. To confirm the formation of the complex, the signal/noise ratio was required to be higher than 5. Only K5 derivatives that showed binding in this initial step were further analyzed to determine their binding affinity (K_d) for spike. For this purpose, 16 × 1:1 dilution of each K5 derivative were prepared in PBST buffer. Each dilution was mixed with one volume of labeled spike (final spike concentration equal to 25 nM and final ligand concentrations ranging from 15 nM to 500 μM). After 30 min. incubation followed by centrifugation at 10,000 × g for 10 min., samples were loaded into capillaries and MST was measured as described. Data from two to three independently pipetted measurements were analyzed using the MO.Affinity Analysis software version 2.3 (NanoTemper Technologies) using the signal from an MST-on time of 5 s.

Surface plasmon resonance (SPR) assays: a BIAcore X100 instrument (Cytiva) was used. SPR was exploited to measure changes in refractive index caused by the ability of the different sulfated K5 derivatives to prevent the binding of spike to heparin or ACE2 immobilized on a biosensor. Carboxy-methylated dextran CM5 and SA sensor chips, 1-ethyl-3-(3-diaminopropyl)-carbodiimide hydrochloride (EDC) and N-hydroxysuccinimide (NHS) were from Cytiva.

Heparin biosensor: the spike-heparin interaction has been already characterized in a SPR setup[16]. The same experimental conditions were adopted here to evaluate the capacity of sulfated K5 derivatives to prevent the binding of spike to surface-immobilized heparin. A research grade sensor chip SA (Cytiva), coated with a carboxy-methylated dextran matrix pre-immobilized with streptavidin, was used. The first flow cell of the sensor chip was conditioned with three consecutive 1-min. injections of 1.0 M NaCl in 50 mM NaOH. Then, heparin that had been biotinylated at its reducing end was diluted at 0.015 mg/ml in 10 mM HEPES buffer, pH 7.4, containing 150 mM NaCl, 3 mM EDTA, and 0.005% surfactant P20 (HBS-EP) and injected over the activated surface for 8 min at a flow rate of 5.0 μL/min, allowing the immobilization of 120 resonance units (RU) (equal to 9 femtomoles/mm^2) of the GAG. The second flow cell of the sensor chip was coated with biotinylated BSA protein as described above, allowing the immobilization of 569 RU (equal to 9 femtomoles/mm^2) of protein, and used to evaluate the nonspecific binding and for blank subtraction. For binding analysis, the different GAGs described in Table S2 and S3 were diluted in HBS-EP to concentrations ranging between 0.01 to 10,000 nM in the absence or presence of spike protein (45 nM) and injected at a flow rate of 30 μl/min. and at a temperature of 20 °C. The complex was allowed to associate and dissociate for 120 and 300 s, respectively. At the end of the dissociation phase, the surfaces were regenerated with a 60 s injection of 0.25% SDS.

ACE2 biosensor: ACE2 was immobilized on one of the two flow cells of a CM5 sensor chip by standard amine-coupling chemistry as described in Rusnati et al.[54]. BSA was immobilized on the second flow cell which was used for blank subtraction. Different sensor chips were prepared and used for the analyses with the amount of immobilized ACE2 and BSA ranging from 2400 to 7300 RU (equal to 19 to 24 femtomoles/mm^2) and 1600 to 1,3000 RU (equal to 22 to 186 femtomoles/mm^2) of the two proteins, respectively. For binding analysis, heparin (used as a reference compound) and the K5 derivatives selected from the previous screening performed on the heparin biosensor were diluted in HBS-EP at 1, 10 and 100 μM and injected over the two flow cells in the absence or in the presence of a spike fragment representing its RBD domain (20 nM), as for the heparin biosensor described above. At the end of the dissociation phase, the surfaces were extensively washed until the baseline returned to pre-injection levels.

Furin cleavage assay: the ability of the various GAGs to inhibit spike cleavage at the S1/S2 site by furin was evaluated by using the colorimetric assay "CoviDrop™ SARS-CoV-2 targeted proprotein convertase inhibitor screening fast kit" (Epigentek, County Blvd, Farmingdale NY). Briefly, a 2.0 kDa SARS-CoV-2 spike fragment containing the intact S1/S2 $_{681}$RRAR$_{684}$ HBD is tagged with poly-histidine and biotin at its N-terminus and C-terminus, respectively, and immobilized onto microplate wells through histidine-Ni-NTA. The cleavage of the substrate at the S1/S2 site removes the C-terminal S2 portion linked to biotin, causing a decrease of the signal generated by avidin/biotin binding that is detected by colorimetric reaction measured as absorbance at 450 nm in a microplate spectrophotometer. Furin cleavage inhibition blocks the reduction of the signal. Consequently, the extent of spike cleavage is inversely proportional to the signal intensity. The assay was performed according to the manufacturer's instructions (https://www.epigentek.com/catalog/covidrop-sars-cov-targeted-proprotein-convertase-inhibitor-screening-fast-kit-p-84596.html).

Computational studies

Four different systems were modelled: spike Wuhan-Hu-1 variant fully glycosylated in the closed conformation with (i) three K5OSH or (ii) three K5NOSH chains bound, and in the open conformation with (iii) three K5OSH or (iv) three K5NOSH chains bound, respectively. Atomic coordinates of the complete models of closed and open spike (without the stalk) were retrieved from Paiardi et al.[20]. K5 derivatives of 31 monosaccharides (31mer) were docked onto the spike using the incremental sliding window docking method[55] and the polysaccharide models reported in Figure S24. They spanned from the basic domain in the RBD to the S1/S2 functional site. Corresponding models and simulation trajectories of the closed and open conformation of spike with three heparin chains were retrieved from Paiardi et al.[20] and used for comparison.

All-atom MD simulations were carried out using Amber20[56]. Spike was parametrized using ff14SB[57] and GLYCAM-06j[58] force fields. Sulfated K5 derivatives were parameterized as described previously[55]. All systems were placed in a periodic cubic box solvated using the TIP3P water model[59] with 10 Å between the solutes and the edges of the box. Na+ and Cl- ions were added to the box to neutralize the systems and immerse them in a solvent with an ionic strength of 150 mM. Four replicas for each system were simulated. Each system was energy minimized in 14 consecutive minimization steps, each of 100 steps of steepest descent followed by 900 steps of conjugate gradient, with decreasing positional restraints from 1000 to 0 kcal/mol A^2 on all the atoms of the systems, excluding waters, counterions, and hydrogens, with a cutoff for non-bonded interactions of 8 Å. The systems were then subjected to two consecutive steps of heating, each of 100,000 steps, from 10 to 100 K, and from 100 to 310 K, in an NVT ensemble with a Langevin thermostat. Bonds involving hydrogen atoms were constrained with the SHAKE algorithm[60], and a 2 fs time step was used. The systems were then equilibrated at 310 K in four consecutive steps of 2.5 ns each in the NPT ensemble with a Langevin thermostat with random velocities assigned at the beginning of each step. For each system simulated, four independent replica production runs following the same protocol as for the equilibration were carried out starting from restart files chosen randomly from the last 5 ns of equilibration. During the MD simulations, a cutoff of 8 Å for the evaluation of short-range non-bonded interactions was used, and the Particle Mesh Ewald method was employed for the long-range electrostatic interactions. The temperature was kept constant at 310 K with a Langevin thermostat. Coordinates were written at intervals of 100 ps.

Production simulations for replicas of systems (i), (ii) and (iii) were carried out for up to 1 μs, while for system (iv), simulations were extended up to 1.5 μs.

MD trajectories were analyzed using CPPTRAJ[61] in AmberTools20[61], and molecular graphics analysis was performed using Visual MD[62]. Data obtained were then compared with previous analyses performed for simulations of inactive and active spike in the presence of three heparin chains[20]. For consistency, the analysis was performed using the same scripts and parameters as used by Paiardi et al.[20].

Hydrogen bond (H-bond) analysis was performed using CPPTRAJ[61] along all the trajectories for frames at intervals of 10 ns (coordinates written every 100 ps collected with a stride of 100 frames) and setting 3.5 Å as the upper distance for defining a H-bond between heavy atoms. All the atoms, including the hydrogens, of the systems were considered (Figs. 2a, b, 3a, b and Table S5–S6).

Distances between RBD-loops were computed using CPPTRAJ[61] along all the trajectories. Centroids were calculated for the RBD-Loop4 (residues 495–516) of each spike subunit and the distance between two centroids was computed along the trajectory (Fig. 2c, Figure S12).

Solvent-accessible surface area (SASA) was computed using CPPTRAJ[61] along the trajectory with a van der Waals radius of the solvent probe of 1.4 Å. For the analysis of the receptor-binding residues, all the residues of the RBD (residues 319–541) were considered along the trajectory (Figs. 2d, 3f, Figure S13, Figure S19) while for the S1/S2-HBD site, residues 682 to 685 were considered (Figs. 2e, 3g, Figure S14, Figure S20).

Root mean square deviations (RMSD) were calculated using CPPTRAJ[61] for all C-α atoms of the individual spike subunits—S_A, S_B, S_C—and for all the carbon, oxygen, sulfate, and nitrogen atoms of the K5 derivatives (Figure S6–S9). The RMSDs of the hinge regions were calculated for the C- α atoms of residues 527 to 529 for S_A, S_B, and S_C, separately (Fig. 3c, Figure S16).

Root mean square fluctuations (RMSF) were calculated using CPPTRAJ[61] for all C- α atoms of the individual spike subunits—S_A, S_B, S_C—and for all the carbon, oxygen, sulfate, and nitrogen atoms of the K5 derivatives (Figure S10–S20, Figure S24).

Dihedral principal component analysis (dPCA) was performed using CPPTRAJ[61]. The dihedral covariance matrix and the projection were calculated for the backbone phi/psi angles of residues 527 to 529 of the S_C monomer. The first four eigenvectors and eigenvalues were extracted, and the first two principal components were plotted for all of the systems. All the systems were transformed into the same principal component space to evaluate the variance across the replicas (Fig. 3d, Figure S17).

Essential dynamics analysis was performed using Principal Component Analysis performed along all the trajectories individually with CPPTRAJ[61]. The principal modes of motion were visualized using visual MD[62]. The first normalized eigenvectors were plotted along the trajectory, and the direction of motion was defined by visual inspection (Fig. 3e, Figure S18).

Cells

VeroE6 cells were purchased from the American Type Culture Collection (ATCC; Catalog #CRL-1586) for the syncytia formation assay and from the "Istituto Zooprofilattico Sperimentale della Lombardia e dell'Emilia Romagna" (Brescia, Italy) for infection assays. They were maintained in Dulbecco's Modified Eagle Medium (DMEM, GlutaMAX supplement, 100 U/ml penicillin, 100 μg/ml streptomycin and 10% fetal bovine serum (FBS) Gibco, Thermo-Fisher, Waltham, MA, USA) at 37 °C and 5% CO_2. A549 ACE2-positive (A549 ACE2 +) cells, a kind gift from Dr. Stephen J Elledge (Harvard Medical School, Boston, MA, USA), were cultured in RPMI (Gibco, Thermo-Fisher Scientific) supplemented with 10% FBS and maintained at 37 °C in a humidified atmosphere of 5% CO_2.

Plasmids and antibodies

Plasmid encoding for SARS-CoV-2 Wuhan-Hu-1 spike (YP_009724390.1) was kindly provided by Prof. Dr. Stefan Pöhlmann. For this study, the spike sequence was cloned into pcDNA3.1(+) vector. Plasmid encoding for SARS-CoV-2 Omicron BA.1 spike was kindly provided by Prof. Ralf Bartenschlager and purchased from Addgene (#180375). Empty pcDNA3.1(+) vector was used as a negative control. Immunofluorescence staining for spike was performed with rabbit anti-spike antibody (Abcam, ab272504) for Wuhan-Hu-1 and mouse anti-spike for Omicron BA.1 (BIOZOL, GTX632604). Secondary antibodies, Alexa Fluor 488 goat anti-rabbit or anti-mouse (Invitrogen, A11034 and A11029), were used. For plasmid DNA transfection, TransIT-LT1 Transfection Reagent was used according to the manufacturer's protocol (Mirus Bio LLC).

Cell viability assay

VeroE6 or A549 ACE2+ cells were seeded into 24-well plates (2.5×10^4 cells/well) in the culture medium described above and treated with heparin, K5, K5OSH and K5NOSH (from 10 nM to 100 μM) at 37 °C for 48 h. Cell viability was estimated by measuring the ATP levels using CellTiter-Glo (Promega, Madison, WI, USA). All the experiments were repeated three times.

Syncytia formation assay and automated detection of syncytia

VeroE6 cells were seeded in a 24-well plate (glass bottom) at a seeding density of 0.04×10^6 cells/well. Cells were transfected with 500 ng DNA/well. Empty pcDNA3.1(+) vector was used as a negative control. Heparin or K5 derivatives were added after washing the cells 2x with medium 4–6 h post-transfection. Cells were washed 2x with PBS at 24 h post-transfection and fixed by 4% formaldehyde (Science Services, E15710) diluted in PBS for 15 min. at room temperature (RT). Cells were washed 2x with PBS and permeabilized with 0.25% Triton X-100 in PBS for 10 min. at RT. Cells were washed 3× with PBS and blocked with 2.5% lipid-free BSA in 0.1% Tween-20 in PBS (PBS-T) for 1 h at RT. After blocking and washing, cells were incubated with primary antibody solutions prepared by diluting the antibody 1:1000 in 1% lipid-free BSA in PBS-T (dilution buffer) for 1 h at RT. Cells were washed 3× with PBS and incubated with secondary antibody solutions prepared by diluting antibodies 1:500 in dilution buffer for 1 h at RT in the dark. Cells were washed 3x with PBS and incubated in DAPI (Sigma-Aldrich, D9542, 1:1000 dilution in PBS) for 1 min. at RT. After washing 3x with PBS, plates were imaged in an automated fashion using Cell Discoverer 7 (Zeiss, state, city) with 20x (PLAN-Apo, NA 0.7, air) objective and Zeiss Axiocam 712 mono camera. The entire surface of each well was imaged by tiled acquisition in 3 channels (385 nm LED excitation coupled with 425/30 emission filter for DAPI detection, 470 nm LED excitation coupled with 513/30 emission filter for the spike protein detection and a bright field channel). Individual, tiled images were subsequently stitched covering the entire surface of the well containing approx. 40,000 cells per well on average. To measure the extent of syncytia formation in an unbiased way, we employed an automated image analysis pipeline using the Arivis Vision 4D software (Zeiss). First, we segmented nuclei by applying the Cellpose[63], a pre-trained machine learning model "CP" on the DAPI channel, which resulted in successful nuclei detection even in situations where nuclei were very close to each other, as it is often the case within the syncytia. To detect the boundaries of cells expressing different spike mutants, we trained a dedicated semantic deep-learning model using the Arivis Cloud (Zeiss) platform. For training, we used 10 randomly selected 1000 × 1000 px regions of interest from one well and all 3 acquired channels. Two different models were trained for the detection of the Wuhan-Hu-1 and the Omicron BA.1 spike variants. Segmented objects in close proximity were separated by the application of the watershed algorithm as implemented in the "Splitting" module of the Arivis Vision 4D software. Only those objects larger than 420 μm^2 were considered. Syncytia was defined as any cellular object larger than 2,000 μm^2 and containing at least 2 nuclei. In the final step, all nuclei of the spike-expressing cells were classified as either "in" or "out" of syncytia using the "syncytia criterion" mentioned above. From this analysis, "fusogenicity" was calculated as "% of nuclei in syncytia" by dividing the number of nuclei in syncytia by the total number of nuclei in spike-expressing cells. The same automated acquisition and analysis

pipeline was applied to all the experiments, ensuring an unbiased approach and comparable results.

Infection assay

Infections were carried out as previously described[64,65] using the clinical SARS-CoV-2 isolates belonging to B.1 (GISAID accession number: EPI_ISL_1379197) or Omicron BA.1 (GISAID accession number: EPI_ISL_15700833) lineages[66]. The viruses were propagated in VeroE6 cells and the viral titer was determined by a standard plaque assay. All the experiments were performed with a single viral inoculum. All the infection experiments were carried out in a biosafety level-3 (BLS-3) laboratory at a multiplicity of infection equal to 0.01.

Evaluation of antiviral efficacy was performed on VeroE6 or A549 ACE2+ cells grown to 80–90% confluence and infected at 37 °C for 1 h with the SARS-CoV-2 isolates at a multiplicity of infection equal to 0.01. Then, the virus was removed and cells were washed with PBS at 37°C and cultured with media containing 2% FBS in the presence or the absence of heparin, K5, K5OSH and K5NOSH (from 10 nM to 10 µM). Supernatants were collected for further analysis 48 h post-infection (p.i). Mock-infected cells were processed exactly as the SARS-CoV-2-infected ones, except they were not exposed to the virus.

Plaque Assay was performed on VeroE6 cells seeded at a density of 5×10^5 cells/well in a 12-well plate and incubated at 37 °C for 24 h. Supernatants from infected cells were serially diluted in DMEM without FBS and added to the cells. After 1 h incubation, media were removed and cells were washed with PBS at 37 °C. Then cells were covered with an overlay consisting of DMEM with 0.4% SeaPlaque (Lonza, Basel, Switzerland). Cells were further incubated at 37 °C for 48 h and then fixed with 10% formaldehyde at room temperature for 3 h. Formaldehyde and agarose overlay were removed. Cells were then stained with crystal violet (1% w/v in a 20% ethanol solution), and the viral titer (Plaque Forming Unit, PFU/mL) of SARS-CoV-2 was determined by counting the number of plaques. All the experiments were repeated three times.

Safety comments

No unexpected or unusually high safety hazards were encountered during the biochemical and syncytia formation assays and infection experiments.

Data analysis

GraphPad Prism version 8.4 (GraphPad Software, Boston, Massachusetts USA, www.graphpad.com) was used to perform non-linear regression analysis, plot the dose-response curves and calculate the half-maximal inhibitory concentration (IC_{50}) values for each compound. Student's t-test or one-way ANOVA analysis of variance was performed using Microsoft Excel. Unless otherwise specified, P value was determined by Mann-Whitney test ($^*P < 0.05$; $^{**}P < 0.005$. $^{***}P < 0.0005$).

Data Availability

Data supporting the findings of this study are publicly available in the Zenodo repository [https://doi.org/10.5281/zenodo.15273706). The manuscript has been deposited in the BioRXiv preprint server [https://doi.org/10.1101/2025.04.23.650164).

Received: 6 August 2025; Accepted: 18 November 2025;
Published online: 09 January 2026

References

1. Islam, M. A. A review of SARS-CoV-2 variants and vaccines: Viral properties, mutations, vaccine efficacy, and safety. *Infect. Med. ((Beijing))* **2**, 247–261 (2023).
2. Ke, Z. et al. Structures and distributions of SARS-CoV-2 spike proteins on intact virions. *Nature* **588**, 498–502 (2020).
3. Hoffmann, M. et al. SARS-CoV-2 Cell Entry Depends on ACE2 and TMPRSS2 and Is Blocked by a Clinically Proven Protease Inhibitor. *Cell* **181**, 271–280.e278 (2020).
4. Wrapp, D. et al. Cryo-EM structure of the 2019-nCoV spike in the prefusion conformation. *Science* **367**, 1260–1263 (2020).
5. Walls, A. C. et al. Structure, Function, and Antigenicity of the SARS-CoV-2 Spike Glycoprotein. *Cell* **181**, 281–292.e286 (2020).
6. Yan, R. et al. Structural basis for the recognition of SARS-CoV-2 by full-length human ACE2. *Science* **367**, 1444–1448 (2020).
7. Lan, J. et al. Structure of the SARS-CoV-2 spike receptor-binding domain bound to the ACE2 receptor. *Nature* **581**, 215–220 (2020).
8. Peacock, T. P. et al. The furin cleavage site in the SARS-CoV-2 spike protein is required for transmission in ferrets. *Nat. Microbiol.* **6**, 899–909 (2021).
9. Xu, H. et al. High expression of ACE2 receptor of 2019-nCoV on the epithelial cells of oral mucosa. *Int. J. Oral. Sci.* **12**, 8 (2020).
10. Coutard, B. et al. The spike glycoprotein of the new coronavirus 2019-nCoV contains a furin-like cleavage site absent in CoV of the same clade. *Antivir. Res.* **176**, 104742 (2020).
11. Essalmani, R. et al. Distinctive roles of furin and TMPRSS2 in SARS-CoV-2 infectivity. *J. Virol.* **96**, e0012822 (2022).
12. Johnson, B. A. et al. Loss of furin cleavage site attenuates SARS-CoV-2 pathogenesis. *Nature* **591**, 293–299 (2021).
13. Low, J. S. et al. ACE2-binding exposes the SARS-CoV-2 fusion peptide to broadly neutralizing coronavirus antibodies. *Science* **377**, 735–742 (2022).
14. Kim, S. Y. et al. Characterization of heparin and severe acute respiratory syndrome-related coronavirus 2 (SARS-CoV-2) spike glycoprotein binding interactions. *Antivir. Res.* **181**, 104873 (2020).
15. Clausen, T. M. et al. SARS-CoV-2 Infection Depends on Cellular Heparan Sulfate and ACE2. *Cell* **183**, 1043–1057.e1015 (2020).
16. Liu, L. et al. Heparan Sulfate Proteoglycans as Attachment Factor for SARS-CoV-2. *ACS Cent. Sci.* **7**, 1009–1018 (2021).
17. Paiardi, G., Ferraz, M., Rusnati, M. & Wade, R. C. The accomplices: Heparan sulfates and N-glycans foster SARS-CoV-2 spike:ACE2 receptor binding and virus priming. *Proc. Natl. Acad. Sci. USA* **121**, e2404892121 (2024).
18. Mycroft-West, C. J. et al. Heparin Inhibits Cellular Invasion by SARS-CoV-2: Structural Dependence of the Interaction of the Spike S1 Receptor-Binding Domain with Heparin. *Thrombosis Haemost.* **120**, 1700–1715 (2020).
19. Parafioriti, M. et al. Evidence for Multiple Binding Modes in the Initial Contact Between SARS-CoV-2 Spike S1 Protein and Cell Surface Glycans. *Chemistry* **29**, e202202599 (2023).
20. Paiardi, G. et al. The binding of heparin to spike glycoprotein inhibits SARS-CoV-2 infection by three mechanisms. *J. Biol. Chem.* **298**, 101507 (2022).
21. Kim, S. H. et al. GlycoGrip: Cell Surface-Inspired Universal Sensor for Betacoronaviruses. *ACS Cent. Sci.* **8**, 22–42 (2022).
22. Kim, S. H. et al. SARS-CoV-2 evolved variants optimize binding to cellular glycocalyx. *Cell Rep. Phys. Sci.* **4**, 101346 (2023).
23. Froese, J. et al. Evolution of SARS-CoV-2 spike trimers towards optimized heparan sulfate cross-linking and inter-chain mobility. *Sci. Rep.* **14**, 32174 (2024).
24. Eilts, F. et al. The diverse role of heparan sulfate and other GAGs in SARS-CoV-2 infections and therapeutics. *Carbohydr. Polym.* **299**, 120167 (2023).
25. Jiang, L. et al. Heparin mimetics as potential intervention for COVID-19 and their bio-manufacturing. *Synth. Syst. Biotechnol.* **8**, 11–19 (2023).
26. Mangiafico, M., Caff, A. & Costanzo, L. The Role of Heparin in COVID-19: An Update after Two Years of Pandemics. *J. Clin Med*. **11**, https://doi.org/10.3390/jcm11113099 (2022).
27. Rusnati, M., Oreste, P., Zoppetti, G. & Presta, M. Biotechnological engineering of heparin/heparan sulphate: a novel area of multi-target drug discovery. *Curr. Pharm. Des.* **11**, 2489–2499 (2005).
28. Casu, B., Petitou, M., Provasoli, M. & Sinaÿ, P. Conformational flexibility: a new concept for explaining binding and biological

properties of iduronic acid-containing glycosaminoglycans. *Trends Biochem Sci.* **13**, 221–225 (1988).
29. Hagner-Mcwhirter, A., Lindahl, U. & Li, J. Biosynthesis of heparin/heparan sulphate: mechanism of epimerization of glucuronyl C-5. *Biochem J.* **347**, 69–75 (2000).
30. Gori, A. M. et al. Cytokine gene expression and production by human LPS-stimulated mononuclear cells are inhibited by sulfated heparin-like semi-synthetic derivatives. *J. thrombosis Haemost. JTH* **2**, 1657–1662 (2004).
31. Jerabek-Willemsen, M., Wienken, C. J., Braun, D., Baaske, P. & Duhr, S. Molecular interaction studies using microscale thermophoresis. *Assay. drug Dev. Technol.* **9**, 342–353 (2011).
32. Seidel, S. A. et al. Microscale thermophoresis quantifies biomolecular interactions under previously challenging conditions. *Methods* **59**, 301–315 (2013).
33. Nie, C. et al. Polysulfates Block SARS-CoV-2 Uptake through Electrostatic Interactions*. *Angew. Chem. Int Ed. Engl.* **60**, 15870–15878 (2021).
34. Braun, E. & Sauter, D. Furin-mediated protein processing in infectious diseases and cancer. *Clin. Transl. Immunol.* **8**, e1073 (2019).
35. Schuurs, Z. P. et al. Evidence of a putative glycosaminoglycan binding site on the glycosylated SARS-CoV-2 spike protein N-terminal domain. *Computational Struct. Biotechnol. J.* **19**, 2806–2818 (2021).
36. Buchrieser, J. et al. Syncytia formation by SARS-CoV-2-infected cells. *EMBO J.* **39**, e106267 (2020).
37. Krylova, N. V. et al. Carrageenans and the carrageenan-echinochrome complex as anti-SARS-CoV-2 agents. *Int. J. Mol. Sci.* **26**, https://doi.org/10.3390/ijms26136175 (2025).
38. Froba, M. et al. Iota-Carrageenan Inhibits Replication of SARS-CoV-2 and the Respective Variants of Concern Alpha, Beta, Gamma and Delta. *Int. J. Mol. Sci.* **22**, https://doi.org/10.3390/ijms222413202 (2021).
39. Guimond, S. E. et al. Synthetic heparan sulfate mimetic pixatimod (PG545) potently inhibits SARS-CoV-2 by disrupting the spike-ACE2 interaction. *ACS Cent. Sci.* **8**, 527–545 (2022).
40. Bertini, S. et al. Pentosan polysulfate inhibits attachment and infection by SARS-CoV-2 in vitro: insights into structural requirements for binding. *Thrombosis Haemost.* **122**, 984–997 (2022).
41. Sun, L. et al. Well-defined heparin mimetics can inhibit binding of the trimeric spike of SARS-CoV-2 in a length-dependent manner. *JACS Au* **3**, 1185–1195 (2023).
42. Chen, D., Zhao, Y. G. & Zhang, H. Endomembrane remodeling in SARS-CoV-2 infection. *Cell Insight* **1**, 100031 (2022).
43. Meng, B. et al. Altered TMPRSS2 usage by SARS-CoV-2 Omicron impacts infectivity and fusogenicity. *Nature* **603**, 706–714 (2022).
44. Zhao, H. et al. SARS-CoV-2 Omicron variant shows less efficient replication and fusion activity when compared with Delta variant in TMPRSS2-expressed cells. *Emerg. Microbes Infect.* **11**, 277–283 (2022).
45. Papa, G. et al. Furin cleavage of SARS-CoV-2 Spike promotes but is not essential for infection and cell-cell fusion. *PLoS Pathog.* **17**, e1009246 (2021).
46. Koch, J. et al. TMPRSS2 expression dictates the entry route used by SARS-CoV-2 to infect host cells. *EMBO J.* **40**, e107821 (2021).
47. Nader, H. B. et al. New insights on the specificity of heparin and heparan sulfate lyases from Flavobacterium heparinum revealed by the use of synthetic derivatives of K5 polysaccharide from E. coli and 2-O-desulfated heparin. *Glycoconj. J.* **16**, 265–270 (1999).
48. Sahin, G. et al. Antivirals and the potential benefits of orally inhaled drug administration in COVID-19 treatment. *J. Pharm. Sci.* **111**, 2652–2661 (2022).
49. Gatti, M. & De Ponti, F. Drug Repurposing in the COVID-19 era: insights from case studies showing pharmaceutical peculiarities. *Pharmaceutics* **13**, https://doi.org/10.3390/pharmaceutics13030302 (2021).
50. van Haren, F. M. P. et al. Inhaled nebulised unfractionated heparin for the treatment of hospitalised patients with COVID-19: A multicentre case series of 98 patients. *Br. J. Clin. Pharm.* **88**, 2802–2813 (2022).
51. Collino, M. et al. Effects of a semi-synthetic N-,O-sulfated glycosaminoglycan K5 polysaccharide derivative in a rat model of cerebral ischaemia/reperfusion injury. *Thrombosis Haemost.* **102**, 837–845 (2009).
52. Oreste, P. & Zoppetti, G. Semi-synthetic heparinoids. *Handb. Exp. Pharmacol.* 403–422, (2012).
53. Manzoni, M., Bergomi, S. & Cavazzoni, V. Production of K5 polysaccharides of different molecular weight by *Escherichia Coli*. *J. Bioact. Compat. Polym.* **11**, 301–311 (1996).
54. Rusnati, M. et al. Cholenic acid derivative UniPR1331 impairs tumor angiogenesis via blockade of VEGF/VEGFR2 in addition to Eph/ephrin. *Cancer Gene Ther.* **29**, 908–917 (2022).
55. Bugatti, A. et al. Heparin and heparan sulfate proteoglycans promote HIV-1 p17 matrix protein oligomerization: computational, biochemical and biological implications. *Sci. Rep.* **9**, 15768 (2019).
56. AMBER 2020 (University of California, San Francisco., 2020).
57. Maier, J. A. et al. ff14SB: improving the accuracy of protein side chain and backbone parameters from ff99SB. *J. Chem. Theory Comput.* **11**, 3696–3713 (2015).
58. Kirschner, K. N. et al. GLYCAM06: a generalizable biomolecular force field. Carbohydrates. *J. Comput. Chem.* **29**, 622–655 (2008).
59. Pekka, M. & Lennart, N. Structure and Dynamics of the TIP3P, SPC, and SPC/E Water Models at 298 K. *J. Phys. Chem. A* **105**, 9954–9960 (2001).
60. Kräutler, V., Van Gunsteren, W. F. & Hünenberger, P. H. Vol. 22 501–508 (Journal of Computational Chemistry, Journal of Computational Chemistry, 2001).
61. Roe, D. R. & Cheatham, T. E. PTRAJ and CPPTRAJ: software for processing and analysis of molecular dynamics trajectory data. *J. Chem. Theory Comput.* **9**, 3084–3095 (2013).
62. Humphrey, W., Dalke, A. & Schulten, K. VMD: visual molecular dynamics. *J. Mol. Graph.* **14**, 27–38 (1996).
63. Stringer, C., Wang, T., Michaelos, M. & Pachitariu, M. Cellpose: a generalist algorithm for cellular segmentation. *Nat. Methods* **18**, 100–106 (2021).
64. Caccuri, F. et al. A persistently replicating SARS-CoV-2 variant derived from an asymptomatic individual. *J. Transl. Med.* **18**, 362 (2020).
65. Caccuri, F. et al. SARS-CoV-2 Infection remodels the phenotype and promotes angiogenesis of primary human lung endothelial cells. *Microorganisms* **9**, https://doi.org/10.3390/microorganisms9071438 (2021).
66. Bugatti, A. et al. SARS-CoV-2 Infects Human ACE2-negative endothelial cells through an α(v)β(3) integrin-mediated endocytosis even in the presence of vaccine-elicited neutralizing antibodies. *Viruses* **14**, https://doi.org/10.3390/v14040705 (2022).

Acknowledgements

We thank the Infectious Diseases Imaging Platform (IDIP) at the Center for Integrative Infectious Disease Research Heidelberg for microscopy support, Glycores 2000. S.r.l for providing the heparin and K5 derivatives and Stefan Richter (HITS) for technical support of the computational work. G.P. and R.C.W. thank the Klaus Tschira Foundation and the Deutsche Forschungsgemeinschaft (DFG, German Research Foundation - Project number: 458623378 to R.C.W.) for support. G.P. was supported by the AI Health Innovation Cluster (postdoc fellowship–1st cohort) and by the Joachim Herz Stiftung (Add-on fellowship for Interdisciplinary LifeScience – 8th cohort). G.P. was supported by the Innogly–Cost Action CA18103 network. The support of the Heidelberg University Flagship Initiative in "Engineering Molecular Systems" is gratefully acknowledged (Project number ExU 6.1.20 (CoVLP) to P.C. and R.C.W.). M.R. thanks Ministero dell'Istruzione, Università e Ricerca (MIUR) (project ex 60%). M.M. thanks the European Union

(NextGenerationEU), Italian NRRP project code IR0000031 - Strengthening BBMRI.it - CUP B53C22001820006. G.P. and R.C.W. gratefully acknowledge the provision of computing resources by HITS and the state of Baden-Württemberg through bwHPC and the German Research Foundation (DFG) through grants INST 35/1134-1 FUGG and INST 35/1597-1 FUGG. This publication was supported through state funds approved by the State Parliament of Baden-Württemberg for the Innovation Campus Health + Life Science Alliance Heidelberg Mannheim. V.L. was funded by Deutsches Zentrum für Infektionsforschung (DZIF), grant number TTU 04.710.

Author contributions

M.M.: methodology, validation, SPR analysis. C.U.: MST and furin cleavage assays, review & editing. L.Z.: methodology, validation, syncytia assays, writing, review & editing. P.O.: resources (glycosaminoglycans). A.Z.: infection assays. A.C.: funding acquisition. F.C.: infection assays, writing original draft. V.L.: methodology, validation. P.C.: methodology, validation, review & editing, supervision, funding acquisition; R.C.W.: conceptualization, resources, review & editing, supervision, funding acquisition. M.R.: conceptualization, resources, writing, review & editing, funding acquisition. G.P.: conceptualization, methodology, validation, investigation, simulations, writing original draft, visualization, review & editing.

Competing interests

The authors declare no competing interests.

Additional information

Supplementary information The online version contains supplementary material available at https://doi.org/10.1038/s44298-025-00163-4.

Correspondence and requests for materials should be addressed to Rebecca C. Wade, Marco Rusnati or Giulia Paiardi.